ORIGINAL ARTICLE

Development of exosome membrane materials-fused microbubbles for enhanced stability and efficient drug delivery of ultrasound contrast agent

Yongho Jang[a,†], Jeehun Park[b,†], Pilsu Kim[c], Eun-Joo Park[d], Hyungjin Sun[e], Yujin Baek[f], Jaehun Jung[a], Tai-kyong Song[c], Junsang Doh[b,f,g,*], Hyuncheol Kim[a,h,*]

[a]Department of Chemical and Biomolecular Engineering, Sogang University, Seoul 04107, Republic of Korea
[b]Research Institute of Advanced Materials (RIAM), Institute of Engineering Research, Seoul National University, Seoul 08826, Republic of Korea
[c]Department of Electronic Engineering, Sogang University, Seoul 04107, Republic of Korea
[d]Biomedical Research Institute & Department of Radiology, Seoul National University Hospital, Seoul 03080, Republic of Korea
[e]Interdisciplinary Program in Bioengineering, Seoul National University, Seoul 08826, Republic of Korea
[f]Department of Materials Science and Engineering, Seoul National University, Seoul 08826, Republic of Korea
[g]Institute of Engineering Research, Bio-MAX Institute, Seoul National University, Seoul 08826, Republic of Korea
[h]Department of Biomedical Engineering, Sogang University, Seoul 04107, Republic of Korea

Abstract Lipid-coated microbubbles are widely used as an ultrasound contrast agent, as well as drug delivery carriers. However, the two main limitations in ultrasound diagnosis and drug delivery using microbubbles are the short half-life in the blood system, and the difficulty of surface modification of microbubbles for active targeting. The exosome, a type of extracellular vesicle, has a preferentially targeting ability for its original cell. In this study, exosome-fused microbubbles (Exo-MBs) were developed by embedding the exosome membrane proteins into microbubbles. As a result, the stability of Exo-MBs is improved over the conventional microbubbles. On the same principle that under the exposure of ultrasound, microbubbles are cavitated and self-assembled into nano-sized particles, and Exo-MBs are self-

---

*Corresponding authors.

E-mail addresses: jsdoh@snu.ac.kr (Junsang Doh), hyuncheol@sogang.ac.kr (Hyuncheol Kim).

†The authors made equal contribution to this work.

assembled into exosome membrane proteins-embedded nanoparticles (Exo-NPs). The Exo-NPs showed favorable targeting properties to their original cells. A photosensitizer, chlorin e6, was loaded into Exo-MBs to evaluate therapeutic efficacy as a drug carrier. Much higher therapeutic efficacy of photodynamic therapy was confirmed, followed by cancer immunotherapy from immunogenic cell death. We have therefore developed a novel ultrasound image-guided drug delivery platform that overcomes the shortcomings of the conventional ultrasound contrast agent and is capable of simultaneous photodynamic therapy and cancer immunotherapy.

1. Introduction

Over the last few decades, phospholipid-based microbubbles (MBs) have become one of the most common commercial ultrasound (US) contrast agents for the diagnosis of various organs and tissues[1–3]. MBs consist of gaseous core (such as perfluorocarbon gas) covered with proteins, polymers or phospholipid[4,5]. Because of the internal gas phase, MBs are compressible, and when exposed to an US field, acoustic pressure causes them to expand and contract[6]. Due to the high echogenicity of microbubbles even under low MI, microbubbles are considered as promising ultrasound contrast agent. Also, the resonance frequency of MBs ranges about 1–10 MHz, which is the typical range of clinical US imaging scanners[7]. Further, MBs have been actively investigated and developed for therapeutic applications, such as drug and gene delivery[8,9]. MBs can be dissipated by oscillation that repeats expansion and contraction under ultrasound, internal gas leakage due to deformation due to shear stress by US mechanical force, and cavitation by strong ultrasound. MBs constituent lipids destroyed in this process form stable structures such as liposomes or micelles. The cavitation of MBs under the exposure of US generates jet-stream and induces temporary pores on the surrounding cell membrane. Therapeutic agents, such as chemical drugs or genetic materials, can be effectively delivered through the temporarily formed pores. This is called the sonoporation effect[10–12]. Therefore, it is possible to improve drug delivery efficacy by inducing the cavitation of MBs in a specific area by external irradiation of US[5].

While there has been much progress of MBs application in diagnosis and drug delivery systems, they are faced with important limitations[13]. One of the main limitations of MBs is their low stability in biological condition, resulting in a short half-life[14,15]. Unlike in storage condition, MBs when injected into the blood vessel are subjected to the flow of blood and higher temperature and pressure. These conditions make the core gas wrapped with phospholipid monolayer rapidly diffuse out, resulting in the collapse of MBs[16]. Therefore, most of the injected MBs are lost in a few minutes, resulting in insufficient US contrast signal. In addition, as a drug delivery system, the rapid collapse of MBs may cause side effects due to the release of the loaded drug outside the target site. Many attempts have been made to improve the stability of MBs through surface modification, such as PEGylation[17,18], or hybridization with different materials[19]. Despite various attempts to improve the stability of MBs, the results have not been satisfactory. Another main limitation of MBs is the difficulty of surface modification. To effectively deliver drugs loaded in MBs to

specific target cells, many studies have attempted to modify the surface of MBs with antibody or ligand[20]. However, the efficiency of surface modification of MBs with targeting materials was low, since it was difficult to conjugate antibody or ligand to unstable MBs, and during fabrication, many MBs were lost[21–23]. Also, surface modification of MBs is too costly, which is a general hurdle for targeted delivery. Therefore, studies using MBs as a targeted drug carrier have not shown satisfactory results.

Exosomes, one of the extracellular vesicles that are released from all types of cells, have membrane structure like cells. With various phospholipids and membrane proteins, the membrane of exosomes is highly stable *in vivo*[24]. So, we developed exosome-fused MBs (Exo-MBs) by embedding exosome membrane proteins into the monolayer of MBs to overcome two limitations of the conventional MBs: (1) low stability, and (2) the difficulty of surface modification for active targeting in US diagnosis and drug delivery. In this study, the improved stability and targeting ability of Exo-MBs, compared to conventional MBs, were verified. As a result, Exo-MBs provided enhanced ability as an US contrast agent, as well as demonstrating improved photodynamic therapeutic effects by efficiently delivering a photosensitizer, chlorin e6 (Ce6), to a tumor. Furthermore, Exo-MBs with improved stability both show a high first-line anti-therapy effect and trigger anti-cancer immune activities by inducing immunogenic cell death (ICD). In this study, through *in vitro* and *in vivo* experiments, we verify the high potential of Exo-MBs as a novel platform for an US imaging and drug delivery system.

2. Materials and methods

2.1. Reagents

Dimethyl sulfoxide (DMSO), methanol, chloroform, and other reagents were purchased from Sigma–Aldrich (St. Louis, MO, USA). The 2-distaeroyl-*sn*-glycero-3-phosphocholine (DSPC) and 1,2-dipalmitoyl-*sn*-glycero-3-phosphoethanolamine-*N*-[methoxy (polyethylene glycol)-2000] (ammonium salt) (DSPE-PEG2000) were purchased from Avanti Polar Lipids, Inc. (Alabaster, AL, USA). Chlorin e6 was purchased from Santa Cruz Biotechnology (Dallas, Texas, USA). The human pancreatic cancer cell line MIA-PaCa-2 was obtained from Korean Cell Line Bank (KCLB, Seoul, South Korea). Cell growth medium (DMEM), fetal bovine serum (FBS), Antibiotic Antimycotic Solution, and other materials for cell culture were purchased from Welgene (Gyeongsangbuk-do, Korea).

2.2. Separation of exosome from MIA-PaCa-2 cells

To separate exosomes from MIA-PaCa-2 cells, the growth medium (DMEM) with 25% of FBS was ultracentrifuged at $100,000 \times g$ for 11 h and filtered with 0.22 μm membrane syringe filter to remove exosomes in FBS. The ultracentrifuged 25% FBS medium was further diluted with DMEM, and antibiotic antimycotic (AA) solution was added to make complete medium of 10% FBS and 1% AA solution. After discarding the growth medium of MIA-PaCa-2 culture and washing, the cells were washed with DPBS twice, then cultured with exosome free medium for 2 days. To harvest MIA-PaCa-2-derived exosomes, the cultured medium was first centrifuged at $300 \times g$ for 10 min to remove floating cells. Next, the supernatant was centrifuged at $2000 \times g$ for 10 min to remove cell debris. Lastly, it was centrifuged at $10,000 \times g$ for 30 min to remove microparticles in the centrifuged medium. Ultracentrifugation was then performed at $100,000 \times g$ for 70 min. The exosome pallet was resuspended and ultracentrifuged using the same conditions. The final pallet was suspended with 1 mL of PBS, and stored in 1.75 mL tube. The same procedure was conducted to collect exosomes derived from B16F10 cells and CT26 cells.

2.3. Manufacturing Exo-MBs

MBs were manufactured using DSPC and DSPE-PEG2000 through a reverse-phase evaporation method[25]. Briefly, lipid mixture (DSPC/DSPE-PEG2k = 9/1, n/n) was dissolved in chloroform at 10 mg/mL. Lipid film were prepared by evaporating chloroform using a nitrogen gas stream, and then dried under vacuum condition for more than 2 h. The lipid film was hydrated and homogenized with phosphate buffered saline (PBS) by sonication over a phase transition temperature of 55 °C. Then, MBs were formed by mechanical agitation for 45 s using VialMix™ activator (Lantheus Medical Imaging, Billerica, MA, USA) post-refill with perfluoropropane gas. Exo-MBs were manufactured through the same procedure, but 20 μg of exosome membrane proteins obtained by sonicating exosomes from MIA-PaCa-2 cells was added, before hydration of the lipid film. For Ce6-loaded Exo-MBs, 0.1 mg of Ce6 dissolved in methanol was added to lipid solution, before evaporation. After the formation of Exo-MBs and MBs, the solution was transferred to 5 mL syringe, and sealed, then centrifuged at $10 \times g$ for 1 min. Floating bubbles were discarded, and the remaining solution was transferred to another syringe, and centrifuged at $100 \times g$ for 1 min. At this point, the floating bubbles were collected with the addition of 1 mL PBS. For confirmation of exosomal membrane protein using Alexa555-NHS dye and loading of Ce6, floated bubbles 1 min after manufacturing Exo-MBs or MBs were discarded and remaining solution was transferred to 5 mL syringe, and centrifuged at $20 \times g$ for 1 min. At this point, the floated bubbles were collected with the addition of 1 mL PBS.

2.4. Characterization of Exo-MBs

The size distribution and zeta-potentials of the particles were analyzed using dynamic light scattering (Zetasizer Nano ZS, Malvern Instruments, Westborough, MA, USA). To confirm the existence of exosome membrane protein on the surface of Exo-MBs, Alexa555-NHS fluorescence dye, which conjugates with the amine group of protein, was used. After Exo-MBs and MBs manufacturing, 2 μL of Alexa555-NHS dye were added.

Unconjugated dye was removed by floating bubbles with centrifuge. Imagery was taken by fluorescence microscopy (Nikon Eclipse TI-DH, Nikon, Japan) using DIC mode and TRITC filter. For the flow cytometry experiment, fluorescent dye-labeled anti-CD9, anti-CD63, and anti-CD81 antibodies were used to investigate the presence of specific exosome membrane proteins in the lipid layer of Exo-MBs. The embedded exosomal membrane protein was measured by BCA protein assay kit. The load of Ce6 into Exo-MBs was confirmed with red-shift of absorbance peak and fluorescence microscopy using DIC mode and Cy5.5 filter.

2.5. Simulation of the resonance frequency of MBs

The resonance frequency of Exo-MBs was determined theoretically, using Eq. (1) [26]:

$$f_{res} = \frac{1}{2\pi R} \sqrt{\left(\frac{3\gamma p_0}{\rho R^3} + \frac{2S_p}{\rho R^3}\right)} \tag{1}$$

where, R, γ, p_0, and ρ represent the radius of Exo-MBs, heat capacity ratio of gas, ambient fluid pressure, and surrounding media density, respectively. The shell thickness of MBs was set at 3 nm[27]. S_p indicates the shell stiffness of Exo-MBs, which was set to 2.5 N/m[28]. The resonance frequency of each sized Exo-MBs was calculated using Eq. (1) with a MATLAB program.

2.6. Measuring the resonance frequency of Exo-MBs

To measure the resonance frequency of Exo-MBs, they were first separated by their size. After discarding large bubbles by centrifugation at $10 \times g$ for 1 min, Exo-MBs of 4 μm in diameter were collected by centrifugation at $20 \times g$ for 1 min. Then, the remaining solution was centrifuged at $50 \times g$ for 1 min to collect 3 μm Exo-MBs. Lastly, the remaining solution was centrifuged at $150 \times g$ for 1 min to collect 2 μm Exo-MBs. Each size group of Exo-MBs was resuspended with 2 mL PBS and centrifuged several times at the respective condition. The final volume of Exo-MBs was 1 mL PBS. We determined the resonance frequency of the Exo-MBs by measuring the frequency-dependent attenuation of the transmitted acoustic signal. First, we calibrated sonicated ultrasound using a needle hydrophone (HNA-0400, ONDA, CA, USA), which helps us to regulate the peak negative pressure regardless of the variations of transducer and sonication frequency (1−20 MHz). The customized acrylamide gel phantom with a hole to contain the Exo-MB solutions was immersed in a water tank filled with degassed water. The phantom was placed in the focal point of ultrasound transducer. The Exo-MBs were injected into the hole of the phantom. The gel phantom was insonated with a peak rarefactional pressure (PRP) of 0.2 MPa to avoid the bubble collapse due to the inertial cavitation. The pulsed ultrasound was sonicated using three single-element ultrasonic transducers. A 2.5 MHz transducer was used to measure US attenuation in the frequency range 1−5 MHz, a 7.5 MHz transducer for 4−10 MHz, and a 15 MHz transducer for 8−20 MHz. In opposite position of US transducer, the hydrophone was located to receive the ultrasound signal. The received signal was captured by 200 MHz of high-speed PC Oscilloscopes (Vitrek, Co., CA, USA) to evaluate the attenuation. The analysis of the received US signals was performed using MATLAB software (The Math Works, Inc., MA, USA). The captured voltage signals were converted into the pressure values by compensating the sensitivity values of the hydrophone according to its frequency. By frequency analysis on

sampled hydrophone data, we measure the magnitude of transmission frequency and calculate the frequency-dependent attenuation by comparing the control data without the phantom and MBs.

2.7. Validation of the enhanced stability of the Exo-MBs

To measure the stability of Exo-MBs, a hemocytometer was used to count Exo-MBs at each time point. The number of Exo-MBs and MBs were measured and the initial number of both Exo-MBs and MBs were matched. At each time point, 10 µL of bubbles were diluted with PBS and the number of bubbles was counted with hemocytometer. For data analysis, the number of Exo-MBs at each point was divided by the initial number of Exo-MBs to normalize the data. A commercial US scanner (Accuvix V10, Samsung Medison Co., Ltd., Seoul, Korea) was used for the visualization of Exo-MBs for the analysis of US imaging properties. The mechanical index was 0.2 and the acquisition time was 29.4 fps. The microbubbles were located at the Tx focal length of 3.5 cm. A linear array transducer with a $5-14$ MHz frequency range was used in the second harmonic mode. The properties of Exo-MBs as US contrast agents were evaluated by measuring and comparing the US signal intensities between Exo-MBs and MBs. The stability of Exo-MBs was evaluated under continuous US radiation for 30 min. The intensity values of the US images were calculated using MATLAB.

2.8. In vitro Exo-MBs cellular uptake with sonoporation effect

The Exo-MBs and MBs were labeled with DiI for cellular uptake imaging. MIA-PaCa-2 cells at 2×10^5 cells per well were seeded on collagen-coated cover glass in 12-well plates. MBs and Exo-MBs were added to each well, and incubated for 30 min. Then, each well was irradiated with US (0.2 W/cm^2, 50% duty cycle) for 10 s. After 3 h of further incubation, each well was washed with DPBS, and fixed with 4% paraformaldehyde for 10 min. After washing out the fixation solution, the cells on the cover glass were mounted using a mounting medium with DAPI (VECTASHIELD, Vector Laboratories Inc., CA, USA), and analyzed by confocal laser scanning microscopy (Leica TCS SP5, Wetzlar, Germany). Quantitative analysis was performed with the same methodology using flow cytometry (FACS AriaII, BD Biosciences, New Jersey, USA).

2.9. Transformation of Exo-MBs to Exo-NPs

To confirm that Exo-MBs were successfully transformed into Exo-NPs after cavitation with US, Exo-MBs were exposed to US (0.2 W/cm^2, 50% duty cycle) for 10 s, and incubated for 1 h. The size of Exo-MBs (before US exposure) and Exo-NPs (after US exposure) were measured using a dynamic light scattering device. To confirm that exosome membrane proteins in Exo-MBs were successfully embedded in Exo-NPs, Exo-NPs were treated with NHS-functionalized Alexa555 fluorescence dye. The image was taken by fluorescence microscopy (Nikon Eclipse TI-DH, Nikon, Japan) using DIC mode and TRITC filter. Also, further exosome membrane protein analysis was conducted with fluorescent-labeled anti-CD9, anti-CD63, and anti-CD81 antibodies, and analyzed with flow cytometry. The load of Ce6 into Exo-NPs was confirmed by fluorescence microscopy using DIC mode and Cy5.5 filter. For intracellular uptake of Exo-NPs, 2×10^5 cells per well of MIA-PaCa-2 cells were seeded on collagen-coated cover glass

in 12-well plates. DiI labeled Exo-MBs were exposed to US (0.2 W/cm^2, 50% duty cycle) for 10 s, and incubated for 1 h. DiI-labeled Exo-NPs transformed from DiI-labeled Exo-MBs and exosome labeled with the same amount of DiI were added to each well and incubated for 3 h. Each well was washed with DPBS, and fixed with 4% paraformaldehyde for 10 min. After washing out the fixation solution, the cytoskeleton of cells was stained. After another washing out process, the cells on the cover glass were mounted using a mounting medium with DAPI (VECTASHIELD, Vector Laboratories Inc., CA, USA), and analyzed by confocal laser scanning microscopy (Leica TCS SP5, Wetzlar, Germany). Quantitative analysis was performed with the same methodology using flow cytometry (FACS Aria II, BD Biosciences, New Jersey, USA).

2.10. In vitro photodynamic therapy of Ce6 loaded Exo-NPs (Ce6-Exo-NPs)

The 1.0×10^4 cells per well of MIA-PaCa-2 cells were seeded into 96-well plates. Cells were washed with DPBS, and incubated for 30 min with 5 µL of MBs, Exo-MBs, Ce6-loaded MBs (Ce6-MBs), and Ce6 loaded Exo-MBs (Ce6-Exo-MBs). The concentration of Ce6 loaded in MBs or Exo-MBs was measured by UV−Vis spectroscopy. The Ce6 concentration of Ce6-MBs and Ce6-Exo-MBs was adjusted to 36.8 µg/mL. Thirty minutes after treating, US (0.2 W/cm^2, 50% duty cycle) was applied to each well for 5 s. After 3 h of incubation, the media was replaced, and laser of 671 nm was irradiated with 100 mW/cm^2 for 10 s per well (Tunable Laser 671 nm, TMA, Seoul, Korea). The amount of ROS in the MIA-PaCa-2 cells was measured by DCFDA Cellular ROS Detection Assay Kit (Abcam, Cambridge, UK), according to the manufacturer's protocol. The level of ROS was assessed 30 min after the laser irradiation. The therapeutic efficacy of Ce6-Exo-NPs was analyzed with the same procedure of measuring ROS generation. After laser irradiation, cells were incubated for 24 h, and cell viability was analyzed with MTT standard protocol. For quantification, 570 nm light absorbance of plate was measured by microplate reader (VERSAmax™, Molecular Devices Corp., Sunnyvale, CA, USA).

2.11. In vivo studies

All in vivo studies conformed to the Guide for the Care and Use of Laboratory Animals published by the National Institutes of Health, USA (NIH publication no. 85-23, 1985, revised 1996), and the mice were maintained under the guidelines of an approved protocol from the Institutional Animal Care and Use Committee (IACUC) of Seoul National University Hospital (Republic of Korea, SNU-220419-3).

2.12. In vivo US imaging of Exo-MBs

Four rats were prepared; each rat was anesthetized using an IP injection of anesthetic solution (Ketamine/Xylazine = 10/1, v/v). A catheter was inserted in the tail vein for the injection of Exo-MBs and other solutions, and 300 µL of MB solution was injected via a syringe with an injection rate of 0.45 mL/min. The mouse aorta was identified and imaged through DC-80 (Mindray, Shenzhen, China), using a 15 MHz transducer. The mechanical index was 1.3 and the frame rate was 29.4 fps. For post-processing analysis, a region of interest (ROI) was drawn within the aorta, such that the ROI was maintained within the aorta for the whole

video loop, ensuring that during respiration motion, the ROI was not sampling tissue outside the aorta.

2.13. In vivo distribution of Ce6-Exo-MBs

Tumor-bearing mice were prepared by subcutaneous injection of 1.0×10^6 B16F10 cells into the left flank of 5-week-old BALB/c nude mice (Orient Bio., South Korea). When the tumor volume reached approximately 100 mm^3, the in vivo distribution of Ce6-Exo-MBs was investigated. Ce6-Exo-MBs (0.1 mg/kg of Ce6) of 100 μL was injected intravenously into the mice ($n = 3$). The tumors were exposed to US (2.0 W/cm, 50% duty cycle, and 1 min per mouse) 10 min after injection. The tumors were extracted and cryo-sectioned 6 h after the injection of the Exo-MBs and US irradiation. The fluorescence images were observed by confocal laser scanning microscopy.

2.14. In vivo therapy and histological analysis of Exo-MBs

In vivo therapy experiment was conducted similarly to the in vivo distribution experiment. However, in the in vivo therapy experiment, treatment was administered twice; the first therapy was administered when the tumor volume reached approximately 100 mm^3, while the second therapy was administered when the tumor volume of the control group reached 500 mm^3. The tumors were laser irradiated (laser power, 100 J/cm^2, 200 mW) with a 670 nm laser immediately after the US irradiation (2.0 W/cm^2, 50% duty cycle, and 1 min per mouse). The tumor sizes were measured by caliper, and the tumor volume was calculated using Eq. (2):

$$\text{Tumor volume} = a^2 \times b/2 \ (a \leq b) \tag{2}$$

where a is tumor width, b is tumor length.

The mice body weights were also measured during the experiment. The mice were sacrificed on Day 27, and the tumors and major organs were extracted for histological analysis. They were embedded in paraffin blocks, and then sectioned in 5 μm thick slices.

2.15. In vivo calreticulin imaging of Ce6-Exo-MBs

CT26 cells were seeded into glass bottom dishes (SPL) with 2 mL of culture media. After 18 h, cells were treated with 50 μL of Exo-MB, Ce6-Exo-MBs, or nothing for 3 h. Then all dishes were exposed to US (0.2 W/cm^2, 80% duty cycle) for 30 s. After changing the media, 671 nm laser was irradiated with 100 mW/cm^2 for 40 s per dish to the corresponding samples. After 5 h incubation, treated cells were stained with primary calreticulin polyclonal antibody (Invitrogen) for 20 min at 37 °C. The Alexa488-labeled secondary polyclonal antibody (Invitrogen) staining was performed for 20 min at 37 °C, after washing twice. Cells were washed with fresh media, and fluorescence was measured by modified IX83 fluorescence microscopy (Olympus) with U-HGLGPS 130 W metal halide lamp and GFP filter set (EX BP 470/40, BS 495, EMBP 525/50).

2.16. ATP release assay

CT26 cells were seeded into 24-well plates (SPL) with 1 mL of culture media. Cells were washed and treated with 12.5 μL of Exo-MB or Ce6-Exo-MB or not, then treated with US (0.2 W/cm^2, 80 duty cycle) for 30 s. After 3 h incubation, all cells were washed

twice with PBS, and changed to 1 mL of serum free media, then treated with 671 nm laser (100 mW/cm^2) for 40 s or not. After 5 h incubation, the supernatants were collected, and centrifuged at $2500 \times g$ at 4 °C for 5 min. Each supernatant (50 μL) was transferred to a black 96-well plate (SPL), and mixed with 50 μL of luciferase reagent in ATP Bioluminescence Assay Kit HS II (Roche). The luminescence was measured by Sense microplate reader (HIDEX).

2.17. In vivo immunotherapeutic efficacy measurement

BALB/c mice (6−8 weeks) purchased from Orient Bio Inc. Gapyeong breeding center and CT26 cells were used to syngeneic mouse tumor model. CT26 cells (0.5×10^6) were subcutaneously injected into the left flank of each mouse. In the distant tumor experiment, CT26 cells (0.5×10^6) were injected subcutaneously into the right flank seven days after the establishment of the primary tumor. Nine days later, the tumors were allowed to reach around 50 mm^3, and mice were randomly divided into 6 groups, of control, aPD-L1, Exo-MB, Exo-MB + aPD-L1, Ce6-Exo-MB, and Ce6-Exo-MB + aPD-L1. Exo-MB and Ce6-Exo-MB (100 μL) were i.v. injected into mice on Days 9 and 16. The tumors were exposed to US (2.0 W/cm^2, 50% duty cycle, and 1 min per mouse) 5 min after injection, and immediately irradiated with 670 nm laser (laser power, 100 J/cm^2, 200 mW). PBS was i.v. injected into the control group. Anti-PD-L1 monoclonal antibodies (10F.9G2, Bioxcell) at 50 μg per mouse were i.p. injected on Days 10, 13, 17, and 20. The tumor volume was calculated according to Eq. (2). For the immune cell analysis, mice were sacrificed on Day 18 to collect tumor and tumor draining lymph nodes. Collected tumor was dissected to around 1 mm^3 fragment, and type I and IV collagenase were treated with 0.2 mg/mL. After incubation in 37 °C, 5% CO$_2$ incubator for 45 min, dissociated cells from the digested tumor were collected. Isolated cells were stained with LIVE/DEAD™ Fixable Near-IR Dead Cell Stain Kit (Cat. L10119, Invitrogen), following the manufacturer's instruction. For the analysis of activated DCs in the tumor draining lymph node, mice were sacrificed one day after PDT treatment. Tumor draining lymph nodes were harvested and grinned on a 40-micron filter to obtain cells that passed through and were used for analysis. CD80 and CD86 double positive DCs were

Table 1 Antibodies used for immune cell analysis.

Analysis	Antibody
M1/M2 ratio	Anti-F4/80-APC (BM8, Invitrogen), anti-CD45-FITC (30-F11, Biolegend), anti-CD163-PE (S15049I, Biolegend), anti-CD11b-BV421 (M1/70, Biolegend), anti-CD86-BV510 (GL1, BD Biosciences)
CD8$^+$ T cell/Treg ratio	Anti-CD4-BV421 (GK1.5, Biolegend), anti-CD25-BV510 (PC61, BD Biosciences), anti-CD45-FITC (30-F11, Biolegend), anti-CD8-PE (53-6.7, Biolegend), anti-FoxP3-PerCPcy5.5 (R16-715, BD Biosciences), anti-CD3-APC (17A2, Biolegend)
Activated dendritic cell analysis	Anti-CD11c-PE-cy7 (XMG1.2, Biolegend), anti-CD45-FITC (30-F11, Biolegend), anti-CD11b-BV421 (M1/70, Biolegend), anti-CD80-APC (16-10A1, eBioscience), anti-CD86-PE (GL-1, Biolegend)

considered as activated. The following antibodies were used for immune cell analysis, as shown in the Table 1. FACS Canto II (BD) was used for the measurement, and Flowjo software was used for the analysis.

2.18. Statistical analysis

All experimental data are presented as the mean ± standard deviation of at least three independent experiments. All the data processing was performed using the ORIGIN® 2018 (Origin Lab Corp., Northampton, MA, USA). Statistical analysis was performed using Student's *t*-test and one-way ANOVA for multiple comparisons. *P*-value less than 0.05 is considered as statistically significant, as noted in the figures with asterisks $^{*}P < 0.05$, $^{**}P < 0.01$, and $^{***}P < 0.001$.

3. Results and discussion

3.1. Preparation and characteristics of Exo-MBs

Exosomes were isolated and purified from human pancreatic cancer MIA-PaCa-2 cells. Fig. 1 demonstrates the successful insertion of exosome membrane proteins into the phospholipid monolayer of the MBs. The exosomes showed size distribution of 147.0 ± 49.0 nm and zeta potential of −16.6 ± 0.95 mV (Fig. 1A). These size and zeta potential values are consistent with previously reported exosome-related data[29]. The exosomes were sonicated and mixed with phospholipids, which are the main component of MBs, to form exosome membrane proteins embedded MBs (Exo-MBs). The size and zeta potential of Exo-MBs slightly increased from 1.40 ± 0.6 to 1.60 ± 0.57 μm, and from −14.8 ± 0.91 to −13.6 ± 0.42 mV, respectively, compared to MBs, of which increases are not significant. The exosomal membrane proteins embedded into Exo-MBs were quantified by BCA protein assay. The initial exosomal membrane protein added to lipid solution was 20 μg and the embedded exosomal membrane protein was measured as 6.4 ± 0.4 μg. Supporting Information Fig. S1 shows transmission electron microscope imagery of the Exo-MBs. Embedment of exosome membrane protein did not alter the MBs' morphology. However, we could not visually confirm by TEM image whether exosome membrane proteins were embedded into the lipid layer of Exo-MBs. Fluorescence images using an amine-reactive fluorescent dye were used to confirm the embedment of the exosome membrane proteins in the phospholipid monolayer of Exo-MBs (Fig. 1B). Since the phospholipids that make up the MBs do not react with the −NHS functional group, the fluorescent dye was only conjugated to the amine group of exosome membrane proteins. Unlike the MBs (Fig. 1B, top row), the red fluorescence signal was observed in the Exo-MBs (Fig. 1B, bottom row), indicating the existence of exosome membrane proteins in the phospholipid monolayer of Exo-MBs. Furthermore, verification of exosome membrane proteins was conducted with antibodies for exosome biomarkers. The tetraspanins abundantly present in the exosome have been proposed as possible exosome biomarkers. Among tetraspanins, CD9, CD63, and CD81 are specially enriched in the membrane of
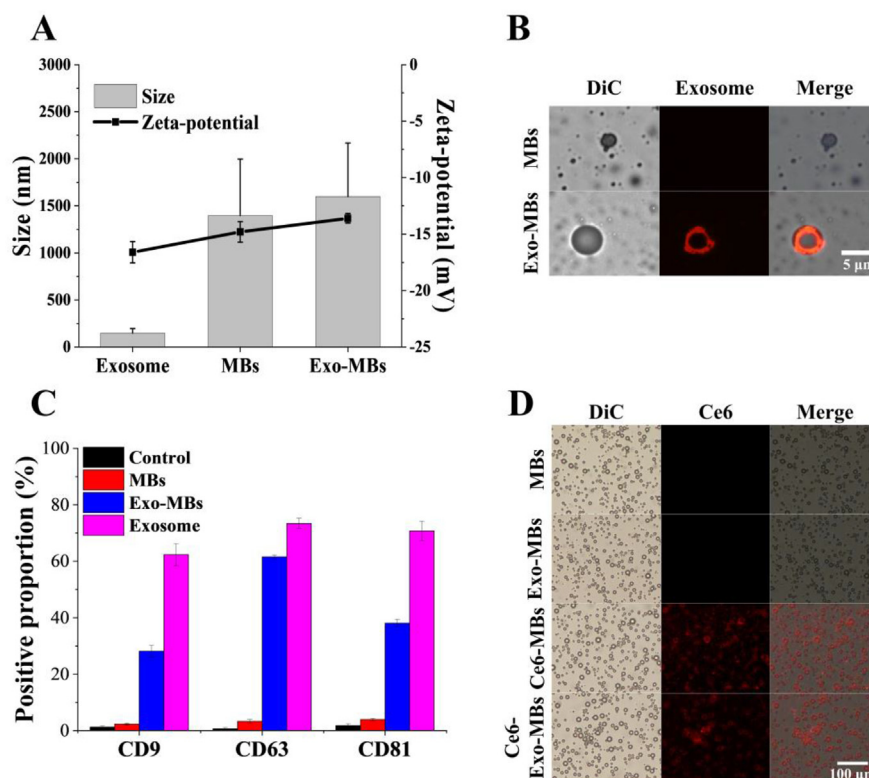

Figure 1 Characteristics of Exo-MBs. (A) Size and zeta potential of exosome, MBs and Exo-MBs. (B) Determination of the embedment of exosome membrane proteins into MBs by fluorescence imagery using an amine-reactive Alexa555 fluorescent dye. (C) Flow cytometry data showing the presence of biomarkers of CD9, CD63, and CD81 in Exo-MBs. (D) Fluorescence microscopy images demonstrating the encapsulation of Ce6 into Exo-MBs.

exosomes[30]. The presence of biomarkers of CD9, CD63, and CD81 in the Exo-MBs was analyzed by flow cytometry to determine the successful embedment of exosome membrane proteins into MBs (Fig. 1C, and Supporting Information Fig. S2). As a result, tetraspanins were determined to be successfully embedded in the phospholipid monolayer of Exo-MBs. Membrane proteins are unstable in aqueous solution, and tend to be embedded in the phospholipid bilayer, like the plasma membrane[31]. This might explain the successful integration of exosome membrane proteins into the phospholipid layer of the MBs. However, we could not determine whether exosome membrane proteins were embedded with the right orientation. Further studies are required to confirm the orientation of exosome membrane proteins, and whether exosome membrane proteins are stably embedded. For therapy studies, Ce6, which is a hydrophobic photosensitizer, was loaded into Exo-MBs. The encapsulation of Ce6 was determined using Ce6-induced fluorescence imaging and UV−Vis spectrometry (Fig. 1D, and Supporting Information Fig. S3).

3.2. Capabilities of Exo-MBs as US contrast agent

After embedding exosome membrane proteins in conventional MBs, changes in the contrast capability of Exo-MBs as an US contrast agent were investigated. One of the important factors as an US contrast agent is resonance frequency. Matching the resonance frequency of the MBs to the irradiated US frequency provides several advantages in medical imaging and externally US triggered drug delivery. The resonance frequency of the MBs is determined by various parameters, among which the most important factors are the shell stiffness and size of the MBs[32]. Therefore, the resonance frequencies of different sized MBs and Exo-MBs were measured (Fig. 2A, and Supporting Information Fig. S4). The experimentally determined resonance frequency values according to the size of MBs and Exo-MBs (Fig. 2A, dots) were found to be not significantly different from the theoretical values (Fig. 2A, solid line), indicating no significant difference in shell stiffness between the MBs and Exo-MBs, and consequently no significant difference in US contrast capability between the MBs and Exo-MBs. This means that the insertion of exosome membrane proteins into the phospholipid monolayer of MBs did not make a significant difference to the stiffness of the phospholipid monolayers of Exo-MBs. Since the US imaging signal is maximized in the resonance frequency range, Exo-MBs could efficiently enhance US signals like conventional MBs using the currently available ultrasonic transducer. Successful embedment of exosome membrane proteins into the phospholipid layer of the MBs improved the stability of the Exo-MBs. Measurement of the change in the number of MBs and Exo-MBs over time confirmed that in comparison to MBs, the stability of Exo-MBs had improved (Fig. 2B). The number of MBs had drastically decreased over time, and after 40 h, no MBs were observed. On the other hand, during the first few hours, the number of Exo-MBs decreased at the same rate as MBs; but after 6 h, the decrease rate was reduced. About 70% of Exo-MBs were still observed even at 40 h, when no MBs had lasted; and more than 40% of Exo-MBs lasted for 72 h. The enhanced stability of Exo-MBs under the exposure of US was further confirmed by placing the Exo-MBs and MBs in phantom made with agarose gel and collecting their US images for 30 min with the continuous exposure of US (Fig. 2C). Fig. 2D is a quantitative graph of the contrast-to-noise ratio value (CNR) from Fig. 2C. Starting with similar CNR value,

MBs lost their US contrast ability within 15 min under the continuous exposure of US, whereas Exo-MBs retained US contrast ability for more than 30 min, even though the contrast signal of Exo-MBs was also greatly decreased. Overall, Fig. 2 demonstrates that Exo-MBs have a more stable phospholipid monolayer, and their US contrast capability lasts longer than that of MBs, without affecting the contrast performance. The stability of MBs has been reported to be improved by surface modification using polyethylene glycol (PEG) polymer (PEGylation) to produce steric hindrance between MBs[33]. By the same principle, the embedment of exosome membrane proteins into MBs could also produce steric hindrance and prevent the coalescence of MBs. Additionally, it has also been reported that cell membrane proteins play a crucial role in controlling cell membrane rigidity and stability[34,35]. However, cells and exosomes have a phospholipid bilayer membrane, while Exo-MBs have a phospholipid monolayer membrane. Further studies are required to investigate how the exosome membrane proteins are stably embedded into the phospholipid monolayer of an MB.

3.3. Determination of enhanced intracellular delivery efficacy of drug-loaded Exo-MBs

As the stability of Exo-MBs are improved over conventional MBs, Exo-MBs have longer half-life. Whether the improved stability of Exo-MBs leads to enhancement in intracellular drug delivery was determined. A hydrophobic fluorescent dye, DiI, was loaded as a drug surrogate into MBs and Exo-MBs, respectively. The US was applied at 30 min after treating MIA-PaCa-2 cells with Exo-MBs or MBs. The degree of intracellular uptake was analyzed qualitatively and quantitatively (Fig. 3). Fig. 3A demonstrates that Exo-MBs delivered fluorescent dye more effectively to MIA-PaCa-2 cells than did MBs. The intracellular delivery capability of Exo-MBs or MBs to MIA-PaCa-2 cells was also quantitatively determined using flow cytometry (Fig. 3B and C). The criterion for drug-delivered cells was set to the point of fluorescence of the 99th percentile of cells of control group. The percentage of positive cells in the free dye group and MBs group were 7.04% and 31.8%, respectively. Inertially cavitated MBs or Exo-MBs self-assemble to liposomes or micelles for thermodynamic stability. Higher delivery efficiency of MBs over the free dye group can be explained by the capability of lipid-based carriers in drug delivery[36]. However, the fluorescence positive cell percentage in Exo-MBs group was 78.6%, indicating the much higher drug deliver efficiency of Exo-MBs. Fig. 2 shows that Exo-MBs revealed improved stability with the help of exosome membrane proteins. More Exo-MBs have remained over MBs after 30 min of incubation, because of the enhanced stability of Exo-MBs. Therefore, more Exo-MBs could be affected by external US, resulting in much enhanced delivery efficiency by the sonoporation effect. However, Exo-MBs were introduced through blood vessel, but most of the target cells which drug loaded in Exo-MBs has to be delivered were located outside of blood vessels.

3.4. Conversion of Exo-MBs to Exo-NPs under the exposure of US

Since most target cells were located out of blood vessel, MBs should be extravasated out of blood vessels for effective delivery. However, micro-sized MBs cannot pass through the vessel wall. On the other hand, it is well known that MBs cavitate inertially, and self-assemble into nano-sized liposomes or micelles that
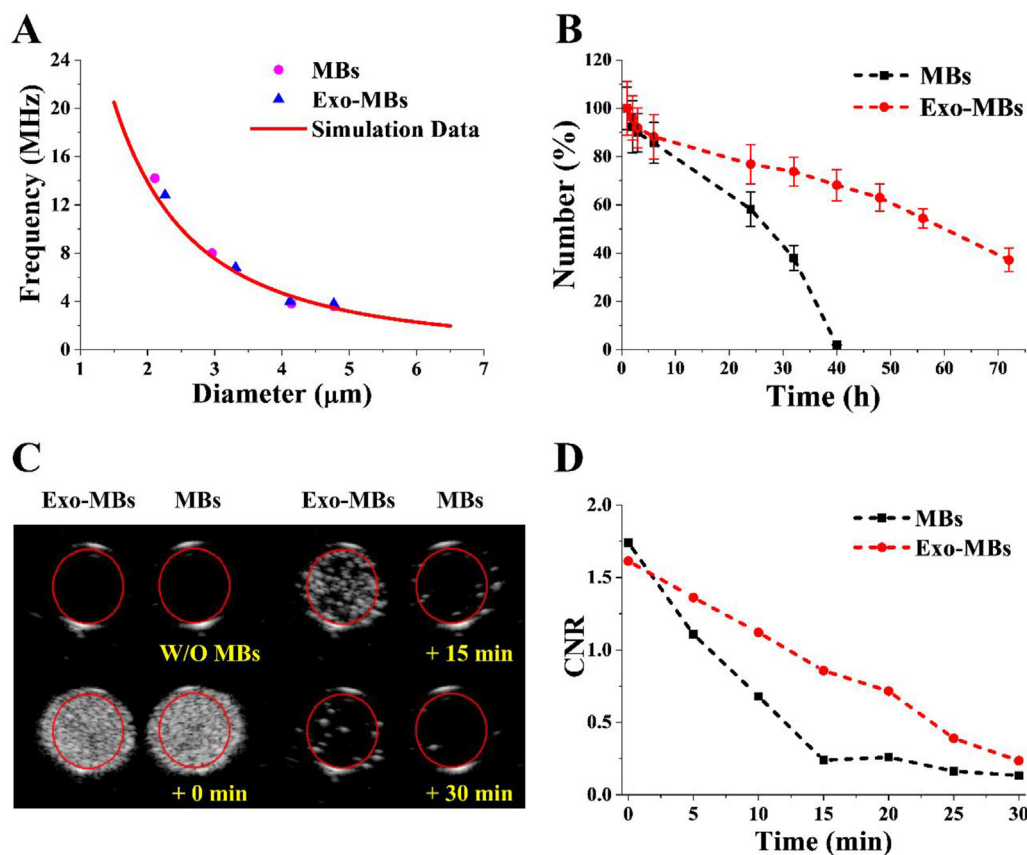
Figure 2 Physical properties of MBs and Exo-MBs as an ultrasound (US) contrast agent. (A) Resonance frequency of MBs and Exo-MBs. Red solid line means theoretical resonance frequency of MBs. (B) Changes in the number of MBs and Exo-MBs over time. (C) US images of MBs and Exo-MBs over 30 min under the exposure of US. (D) Quantitative graph of the contrast-to-noise ratio value (CNR) of US images.

can be extravasated out of the blood circulation under US irradiation[37,38]. Exo-MBs were sonicated to confirm whether they successfully re-assembled into liposomes or micelles. After US irradiation, the sizes of Exo-MBs and MBs changed from 2.06 ± 0.83 to 145 ± 69 nm (Exo-NPs), and from 1.39 ± 0.60 to 101 ± 33 nm (Nanoparticles), respectively (Fig. 4A). During the re-assembly from micro-sized Exo-MBs to nano-sized Exo-NPs under the exposure of US, fluorescence images using an amine-reactive fluorescent dye were used to determine whether the exosome membrane proteins in the Exo-MBs were self-embedded into Exo-NPs (Fig. 4B, and Supporting Information Fig. S5). Unlike the nanoparticles, the red fluorescence signals were observed in Exo-NPs and exosomes. In addition, tetraspanins (CD9, CD63, and CD81) in the Exo-MBs were also self-embedded into the phospholipid layer of Exo-NPs during self-assembly after cavitation of the Exo-MBs (Supporting Information Fig. S6). The above results confirmed that Exo-MBs were successfully re-assembled into Exo-NPs, which have exosome membrane proteins in the phospholipid bilayer. Also, fluorescence microscopy and UV–Vis spectrometry confirmed the self-encapsulation of hydrophobic Ce6 in re-assembled Exo-NPs after cavitation of the Ce6-Exo-MBs (Fig. 4C, and Supporting Information Fig. S7). Ce6 was successfully loaded into the phospholipid bilayer of both re-assembled Ce6-NPs and Ce6-Exo-NPs after US irradiation. It was confirmed that Exo-NPs with exosome membrane proteins was effectively delivered intracellularly like exosomes (Fig. 4D, and Supporting

Information Fig. S8). Overall, Ce6-Exo-MBs with long half-life circulate in the blood vessel and are cavitated by external US irradiation. In this process, cavitated Ce6-Exo-MBs are re-assembled to Ce6-Exo-NPs that contain exosome membrane proteins and Ce6, which was in Ce6-Exo-MBs. Then, nano-sized Ce6-Exo-NPs were extravasated out of the blood vessels and delivered intracellularly. As Exo-MBs were more stable than MBs, more Exo-MBs could be re-assembled to Exo-NPs, resulting in higher drug delivery efficiency.

3.5. ROS generation and the photodynamic therapy of Ce6-Exo-MBs

The higher drug delivery efficiency of Exo-MBs leads to higher therapeutic efficacy. As we loaded Ce6 into Exo-MBs, we conducted photodynamic therapy to confirm whether Exo-MBs could kill tumor cells better than MBs. To verify the generation of reactive oxygen species (ROS) from Ce6 delivered into the cells, Dichlorofluorescin diacetate (DCFDA) cellular ROS detection assay was conducted (Fig. 5A). Without laser irradiation (Laser−), no statistically significant difference was confirmed in intracellular ROS levels between all groups. On the other hand, after exposure to laser (Laser +), the Ce6-loaded nanoparticles (Ce6-NPs) and Ce6-loaded Exo-NPs (Ce6-Exo-NPs) groups showed 1.82- and 2.58-fold increase of fluorescence intensity, respectively, in comparison to the control group. Fig. 4, which
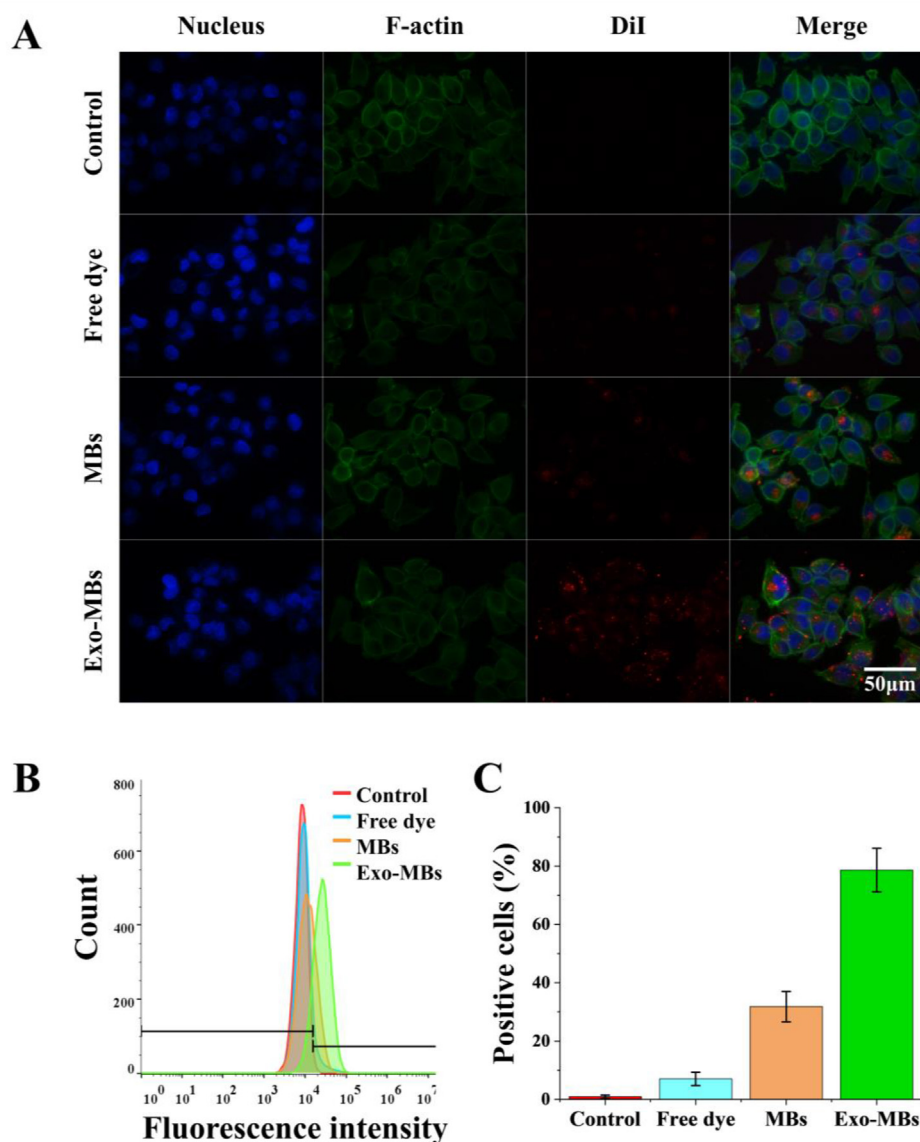
Figure 3   Cellular uptake of Exo-MBs. (A) Confocal microscopy images of MIA PaCa-2 cells treated with Exo-MBs or MBs. Nuclei (blue), F-actin (green), and DiI (red). (B) Quantification of uptake efficiency of Exo-MBs with flow cytometry. (C) Fluorescence positive cell percentage from flow cytometry analysis.

shows the higher intracellular delivery efficiency of Exo-MBs than MBs under the exposure of US, indicates that Ce6-Exo-MBs can be expected to deliver Ce6 into cells more effectively than can Ce6-MBs. Next, we determined whether Ce6-Exo-NPs have higher therapeutic efficacy than Ce6-NPs. In the absence of laser irradiation, there was no significant effect on cell viability, because of insufficient ROS generation (Fig. 5B). The cell viability in the Ce6-NPs treated groups with laser irradiation was slightly reduced from $95.6 \pm 10.9\%$ to $82.2 \pm 10.2\%$. However, the cell viability in the Ce6-Exo-NPs treated group after laser exposure was significantly lowered from $90.4 \pm 9.2\%$ to $34.7 \pm 8.4\%$. As Ce6-Exo-MBs have delivered more Ce6 to the cells, more ROS have been generated, resulting in higher photo-dynamic therapeutic efficacy. Considering the dosage of Ce6 (1.84 µg/mL) used in this experiment, Ce6-Exo-NPs showed high photodynamic therapy efficacy by killing more than 65% of cells, whereas in the Ce6-NPs group, only 10% of cells were killed.

3.6.   In vivo stability of Exo-MBs

To determine whether the stability of Exo-MBs is superior to that of MBs in the actual biological environment, changes in US signal contrast in blood vessels over time were measured after the intravenous injection of Exo-MBs or commercialized US contrast agent, SonoVue®, respectively (Fig. 6 and Supporting Information movie 1). Fig. 6A shows US imagery of the mouse aorta over time. Also, the US signal intensity in the aorta (red circle) was quantified to show the performance of Exo-MBs as an US contrast agent, compared to SonoVue® (Fig. 6B). One minute after intra-venous injection, both Exo-MBs and SonoVue® injected groups showed the highest US signal intensity. The peak enhancements in the Exo-MBs and SonoVue® injected groups were measured to be 146.9 and 132.8, respectively. The US signal intensity decreased over time, with a higher decrease rate in SonoVue® than in Exo-MBs. To validate the superiority of the Exo-MBs over SonoVue®
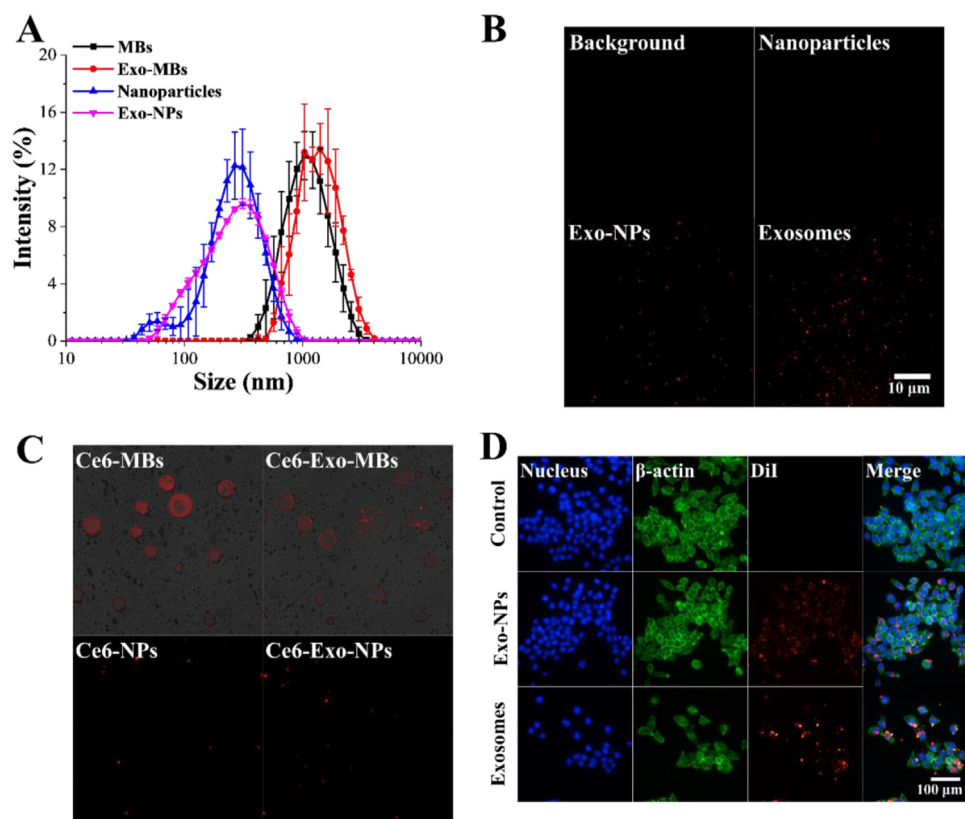
Figure 4 Conversion of Exo-MBs to Exo-NPs and its cellular uptake. (A) Size of Exo-MBs and MBs before and after US irradiation. (B) Verification of exosome membrane proteins using NHS functionalized Alexa555 fluorescence dye. (C) Verification of Ce6 loaded in Exo-NPs using fluorescence microscopy. Fluorescence image of Ce6-MBs and Ce6-Exo-MBs were merged with their DiC image, respectively. (D) Cellular uptake of Exo-NPs and exosomes. Nuclei (blue), cytoskeleton (green), and dye (red).
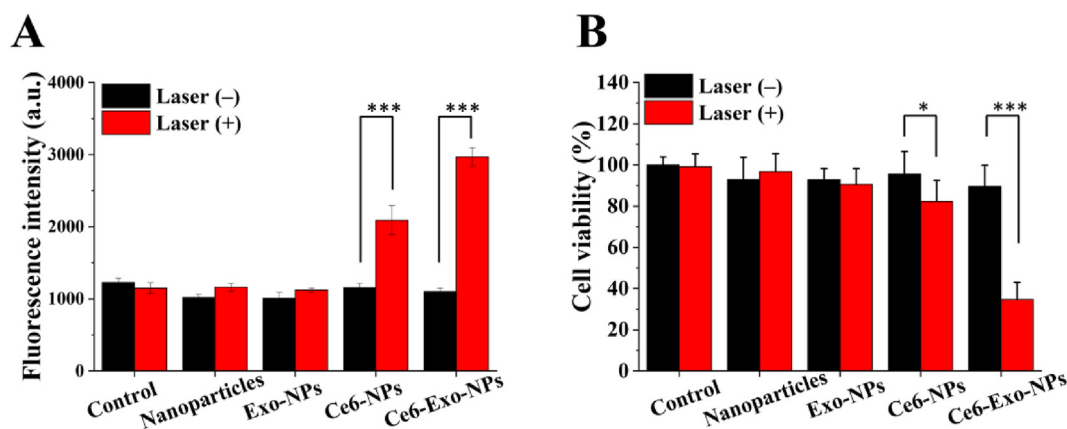

Figure 5 ROS generation and cell viability. (A) Measuring intracellular ROS level treated with Ce6-Exo-NPs by DCFDA assay. (B) Cytotoxicity of Ce6-Exo-NPs with laser irradiation. Data were presented as mean ± SD ($n = 6$). *$P < 0.05$, ***$P < 0.001$ *vs.* indicated.

as an US contrast agent, we analyzed four key parameters (decay rate, area under the curve, peak duration, and time to half-peak) to determine the US contrast agent performance (Fig. 6C, and Supporting Information Fig. S9)[15]. The decay rate values, meaning how fast the contrast agent was washed out as measured by the slope after the peak, of Exo-MBs and SonoVue® were 65.0 and 85.1, respectively. The areas under the curve, meaning the total contrast increase by injected contrast agent as measured by the sums of the US signal intensity, of Exo-MBs and SonoVue® were 392.9 and 280.5, respectively. The peak duration, meaning the length of time the enhanced US signals persist as measured by the time until the contrast decreased to the intensity when injection ended, of Exo-MBs and SonoVue® were 95.1 and 60 s, respectively. The time to half-peak, meaning the time taken for the US signal to reduce to half of the peak intensity, of Exo-MBs and SonoVue® was 180.9 and 93.3 s, respectively. Overall, Exo-MBs
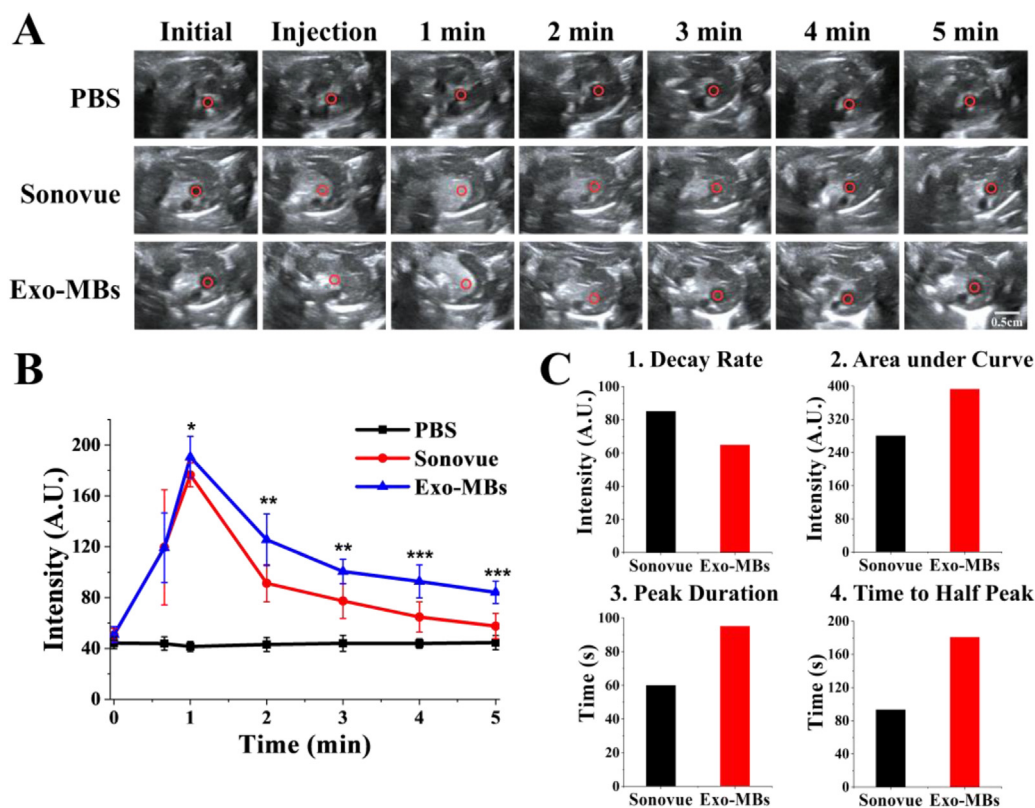
Figure 6 *In vivo* US images of Exo-MBs and SonoVue®. (A) *In vivo* US images around mouse aorta over time. A region of interest (ROI) in the aorta was indicated by a red circle. (B) US signal intensity quantified values in ROI with time. Asterisk (*) denotes the significance between Exo-MBs and SonoVue® injected groups. (C) Four key parameters, decay rate, area under the curve, peak duration, and time to half-peak, calculated from US intensity graph. Data were presented as mean ± SD ($n = 4$). *$P < 0.05$, **$P < 0.01$, ***$P < 0.001$ *vs.* indicated.

and SonoVue® showed similar peak intensity. However, after the peak enhancement, the US signal intensity of Exo-MBs decreased slower than that of SonoVue®, indicating the high stability of Exo-MBs. Therefore, Exo-MBs showed better results in major contrast parameters, demonstrating higher performance as a contrast agent: lower decay rate, and longer US signal enhancement duration. Based on these experimental data, we confirmed that the Exo-MBs are more stable than the conventional MBs in *in vivo*, as well as in *in vitro* conditions. However, unlike the environment in which MBs are placed on the phantom and imaged, intravascularly injected MBs show lower stability due to blood pressure, temperature, flow, and various biomolecules in the blood.

Supporting video related to this article can be found at https://doi.org/10.1016/j.apsb.2023.08.022

3.7. Anti-tumor efficacy of Exo-MBs and histological analysis

To determine the improved therapeutic efficacy of Ce6-Exo-MBs in comparison to Ce6-MBs, either Ce6-MBs or Ce6-Exo-MBs were intravenously administered to B16F10 tumor-bearing BALB/c nude mice ($n = 3$). 10 min post injection, US was applied to the tumor region for 1 min. Six hours after the US exposure, the accumulation of Ce6 in the tumor was determined by fluorescence imagery (Fig. 7A). The Ce6-Exo-MBs injected group demonstrated much higher fluorescence signals from Ce6, compared to the Ce6-MBs injected group. Since Exo-MBs showed

higher stability and improved pharmacokinetics than did MBs in an *in vivo* environment (Fig. 6), Exo-MBs could deliver Ce6, therapeutic agent more effectively into tumor than could MBs. To evaluate the therapeutic efficacy of the Ce6-Exo-MBs, Ce6-MBs and Exo-MBs with or without Ce6 were intravenously administered to B16F10 tumor-bearing BALB/c nude mice ($n = 3$) with the exposure of both US and laser. First therapy was conducted on the day the tumor volume of control group reached 100 mm^3 (Day 6), while second therapy was conducted when the volume of control tumor reached 500 mm^3 (Fig. 7B). Both the Ce6-MBs and Ce6-Exo-MBs treated groups showed high photodynamic therapeutic efficacy, compared to the Ce6 untreated groups (CTRL and Exo-MBs). The enhanced antitumor effects were further microscopically investigated using TUNEL assay. Though both Ce6-MBs and Ce6-Exo-MBs showed excellent tumor volume decrease, the Ce6-Exo-MBs group exhibited more apoptotic cancer cells than the Ce6-MBs, indicating much higher therapeutic potential (Fig. 7C). The weight of each mouse was measured for general toxicity (Fig. 7D). The control and Exo-MBs groups showed increase of weight because of the growth of large tumors. The Ce6-MBs and Ce6-Exo-MBs treated groups showed no significant weight change, demonstrating that the Ce6-Exo-MBs have no severe toxicity. For detailed analysis of the toxicity to major organs and tumors, hematoxylin and eosin (H&E) staining was conducted (Fig. 7E). No group showed cytotoxicity to the major organs. Overall, the Ce6-Exo-MBs reduced tumor growth efficiently, without damaging other organs.
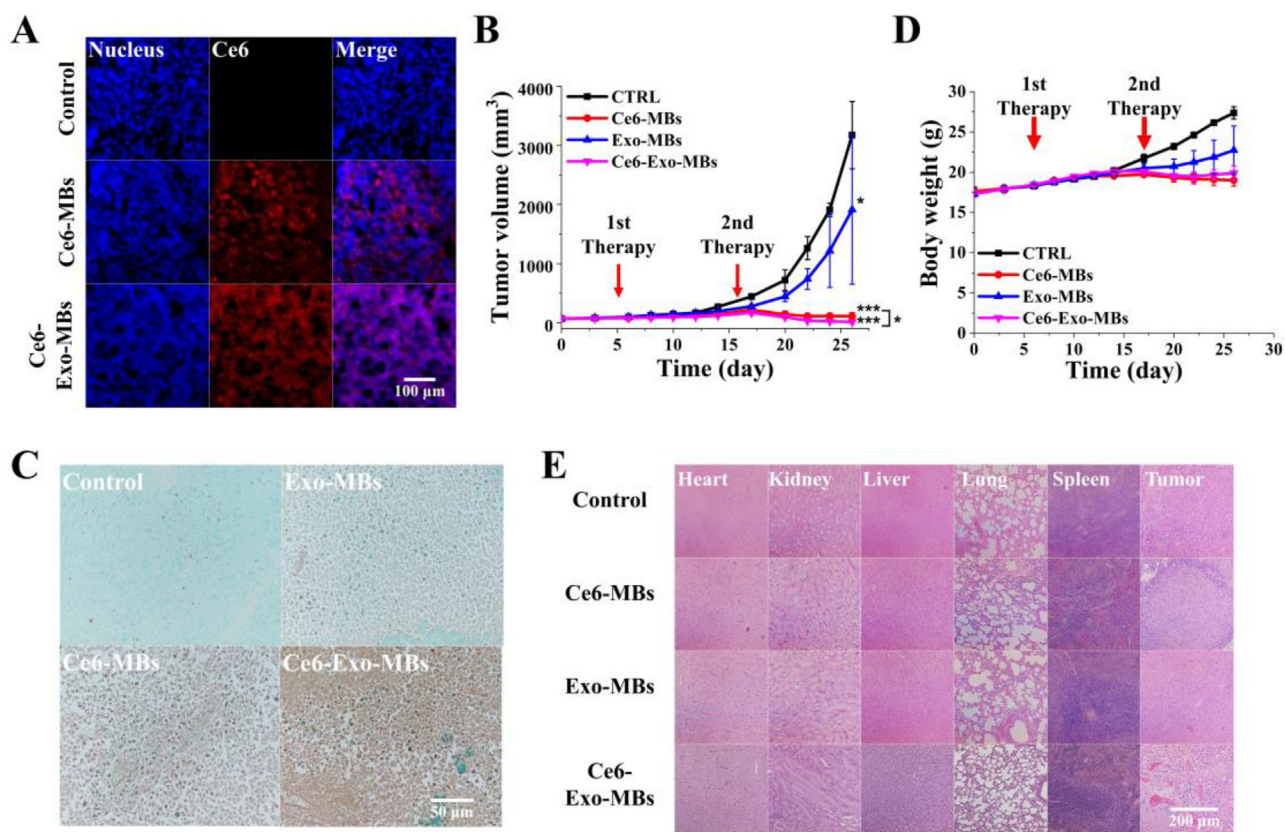
Figure 7 *In vivo* therapeutic efficacy of Exo-MBs. (A) The distribution of Ce6 (red color) in the tumors 6 h after intravenous injection. Blue (DAPI). (B) Tumor volume changes showing the therapeutic efficacy of the Ce6-Exo-MBs with the exposure of both US and laser on Days 6 and 17. (C) TUNEL assay showing apoptotic cells in the tumor after antitumor therapy. (D) Body weight changes during *in vivo* therapy. (E) H&E staining of the major organs after treatment. Data were presented as mean ± SD ($n = 3$). *$P < 0.05$, ***$P < 0.001$ *vs.* indicated.

When the MBs are cavitated under the exposure of US, they generate a jet stream around them, which forms a pore in the blood vessel wall, which is called the sonoporation effect[39]. The nano-sized delivery system, such as re-assembled nanoparticles such as liposomes and micelle from the cavitation of MBs, extravasate effectively from the blood system to the tumor site through the temporary pore in the blood vessel wall. Ce6-Exo-MBs with improved stability are more likely to pass through the blood vessels in or nearby tumors and could be affected by external US irradiation at the tumor region. Simultaneously, Ce6-Exo-MBs were disrupted and re-assembled to Ce6-Exo-NPs. Re-assembled Ce6-Exo-NPs extravasated through the generated pores from the blood circulation to the cancerous tumor site. As more Ce6-Exo-NPs were re-assembled and extravasated, more Ce6-Exo-NPs could effectively accumulate in the tumor (Fig. 7A), delivering much more Ce6 than Ce6-NPs. After laser exposure, the Ce6-Exo-MBs treated group generated more ROS, producing higher photodynamic effects, resulting in greater therapeutic efficacy.

3.8. Immunotherapeutic effect of Ce6-Exo-MBs

Cancer immunotherapy, which activates the patient's immune system to fight against tumor, has drawn great attention[40,41]. Once immunity to a certain cancer has been established, the patient has permanent high resistance to that cancer. Therefore, cancer

immunotherapy can dramatically reduce a recurrence or metastasis. Many studies have reported that PDT induces ICD, resulting in anti-tumor immune activities, and has combination effect with immune checkpoint blockade (ICB) drug[42,43]. To confirm Ce6-Exo-MBs also trigger an anti-cancer immune response, we used syngeneic mouse tumor model having complete immune system. For this, Exo-MBs were prepared using exosome of CT26 mouse colon cancer cell line. Similar to Exo-MBs made with exosomes secreted from human cell line, amine reactive staining confirmed the successful embedment of exosome membrane proteins of exosome markers CD9, CD63, and CD81 into Exo-MBs (Supporting Information Fig. S10A and B). When fluorescent-labeled MBs and Exo-MBs were treated to CT26 cells, the number of fluorescence positive CT26 cells in the Exo-MBs treated group was higher than that of the MBs-treated group, meaning that the targeting ability of exosome was maintained in the Exo-MBs (Fig. S10C−E).

After the CT26 cells were treated with Ce6 encapsulating Exo-MBs (Ce6-Exo-MBs), cell viability was measured with or without laser irradiation (Fig. 8A). Ce6-Exo-MBs with laser irradiation showed outstanding cell death, meaning that PDT was successfully induced. Whether cell death by PDT induced ICD, triggering DC activation, adenosine triphosphate (ATP) release, which leads to DC recruitment, was measured (Fig. 8B). Ce6-Exo-MBs with laser irradiation showed increased ATP level in cell culture media. Also, Calreticulin, which promotes phagocytosis of cancer cells by DCs,
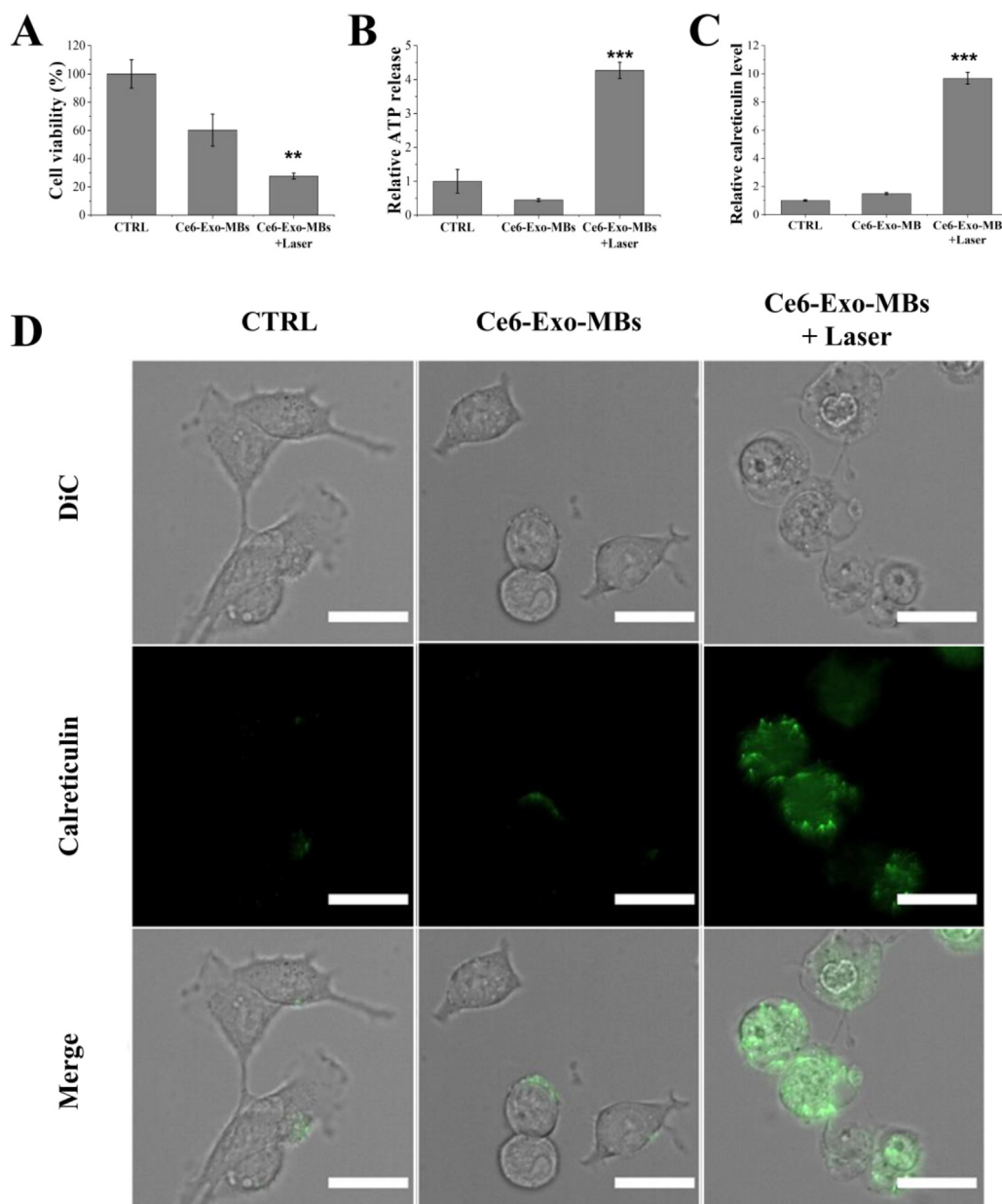
Figure 8 *In vitro* characterizations of the ICD mediated by PDT using CT26 derived Exo-MBs. (A) Cell viability under Ce6-Exo-MBs treatment with laser irradiation. (B) Released ATP amount in the culture media, and (C) cell surface calreticulin after cell death by PDT in the Ce6-Exo-MBs treated group with laser irradiation. (D) Fluorescence images of calreticulin after PDT. Scale bar = 20 μm. Data were presented as mean ± SD ($n = 3$). **$P < 0.01$, ***$P < 0.001$ *vs*. indicated.

was shown to be elevated in the Ce6-Exo-MBs treated group with laser irradiation (Fig. 8C and D). In summary, the PDT efficacy was increased due to the high accumulation of Ce6-Exo-NPs (after US exposure), resulting in high level of ATP release and surface-expressed calreticulin, indirectly showing DC activation.

The effect of increase of ICD was verified in animal model after PDT treatment in the group treated with Ce6-Exo-MBs. It is well known that tumors employ multiple strategies to suppress T-cell-mediated immune responses[44,45]. Immunosuppressive cells, such as regulatory T cells (Treg), tumor-associated myeloid-derived suppressor cells (M-MDSC and PMN-MDSC), or M2-like tumor-associated macrophage (TAM) in tumor microenvironment secrete various factors to evade the immune system. To observe

the ICD effect induced by Ce6-Exo-MBs, aPD-L1 monoclonal antibody (mAb) treatment was combined in CT26 syngeneic mouse tumor model. Like the xenograft results, Ce6-Exo-MBs reduced tumor growth due to the PDT effect (Fig. 9A). However, Ce6-Exo-MBs, together with aPD-L1 mAb, effectively showed further decreased tumor growth without side effect than the single treatment group (Fig. 9A and Supporting Information Fig. S11A). Tumor weight was also the least in the combined treatment (Supporting Information Fig. S12B). Ce6-Exo-MBs treatment increased 40% (10 d) average mouse survival time; however, combination treatment with aPD-L1 increased more than 140% (35 d) (Fig. 9B). We further confirmed the immunotherapeutic effect of Ce6-Exo-MB in a distant tumor model. For this, we first
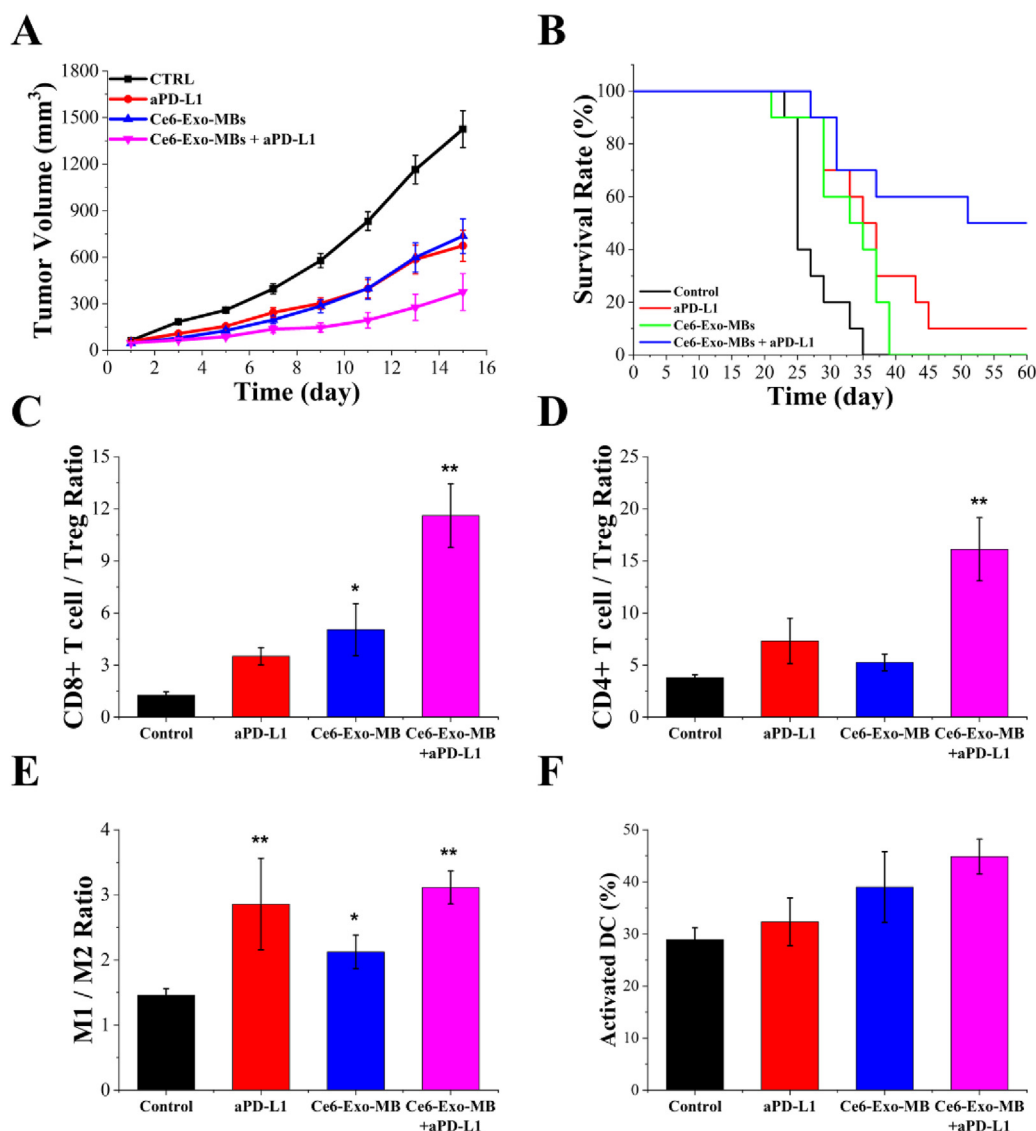
Figure 9 *In vivo* immunotherapeutic efficacy of CT26 derived Exo-MBs. (A) Tumor volume change showing the combination effect of Ce6-Exo-MBs with PD-L1 mAb treatment. (B) tumor bearing mouse survival curves for 60 days. (C) CD8^{+}T/Treg (D) CD4^{+}T/Treg (E) M1/M2 macrophage ratio of tumor infiltrating immune cells. (F) Activated DCs in tumor draining lymph nodes. Data were presented as mean ± SD ($n = 6$). $*P < 0.05$, $**P < 0.01$, *vs.* indicated.

established a primary tumor and then created a distant tumor 6 days later, where only the primary tumor was treated with PDT. Significant suppression of distant tumor formation was observed for both Ce6-Exo-MB monotherapy and combination treatment with anti-PD-L1, indicating the systemic anti-tumor immune responses can be triggered by Ce6-Exo-MB (Fig. S11C and D).

When analyzing tumor infiltrating T lymphocyte, cytotoxic T (CD8^{+}) and immunosuppressive T (Treg) ratio (CD8^{+}/Treg) also increased under combination treatment, meaning that many cytotoxic T cells were recruited to tumor (Fig. 9C, Fig. Supporting Information S12A). CD4^{+} T cell and Treg ratio was also increased under combination treatment, meaning reduced pro-tumoral Treg ratio in tumor infiltrating T lymphocytes (Fig. 9D and Supporting Information Fig. S12A). Anti-tumoral macrophage (M1) to protumoral macrophage (M2) ratio (M1/M2) was also increased, which mean that the immunosuppressive tumor microenvironment was changed (Fig. 9E and Fig. S12B). DC activation in the tumor-

draining lymph nodes was also increased by PDT and anti-PD-L1 combination treatment (Fig. 9F, Fig. S12C), indicating the induction of systemic anti-tumor immune responses. Altogether, our results show that PDT using Ce6-Exo-MBs both killed tumor cells by PDT effect and triggered anti-cancer immune activities by inducing ICD.

4. Conclusions

In this study, Exo-MBs were developed by embedding exosome membrane proteins into MBs, an US contrast agent, to overcome the limitations of conventional MBs, such as the low stability and difficulty of surface modification for active targeting. The Exo-MBs with improved stability demonstrated enhanced US diagnostic feature (Figs. 2 and 6). In terms of drug delivery, MBs were known to be cavitated and self-assembled into nano-sized

particles under the exposure of US. In the process, exosome membrane proteins embedded into Exo-MBs were also embedded into the self-assembled nanoparticles, Exo-NPs (Fig. 4). As more Exo-MBs could be affected by external US because of their stability, more Exo-NPs could extravasate out of blood vessels. Therefore, Exo-NPs demonstrated enhanced intracellular delivery efficiency, resulting in improved photosensitizer treatment efficacy (Figs. 5 and 7). Moreover, ICD induced by photodynamic therapy triggers DC activation, resulting in potential immunotherapeutic effect (Figs. 8 and 9). Thus, Exo-MBs offer great potential as a novel platform for an US imaging and drug delivery system.

Acknowledgments

Author contributions

Yongho Jang, Jeehun Park and Pilsu Kim contributed to the conceptualization; Yongho Jang, Hyungjin Sun, Yujin Baek, Pilsu Kim and Eun-Joo Park contributed to the methodology; Yongho Jang, Eun-Joo Park and Jeehun Park contributed to the data curation; Yongho Jang and Jaehun Jung contributed to the formal analysis; Yongho Jang, Jaehun Jung and Junsang Doh contributed to the preparation of the original draft; and Yongho Jang, Junsang DohJunsang Doh, Tai-kyong Song, Junsang Doh and Hyuncheol Kim contributed to the review and editing. All the authors discussed the results, commented on the manuscript, and approved the final manuscript for publication.

Conflicts of interest

The authors declare no conflicts of interest.

Appendix A. Supporting information

Supporting data to this article can be found online at https://doi.org/10.1016/j.apsb.2023.08.022.

References

1. Klibanov AL. Microbubble contrast agents: targeted ultrasound imaging and ultrasound-assisted drug-delivery applications. *Invest Radiol* 2006;**41**:354−62.
2. Fan CH, Ting CY, Liu HL, Huang CY, Hsieh HY, Yen TC, et al. Antiangiogenic-targeting drug-loaded microbubbles combined with focused ultrasound for glioma treatment. *Biomaterials* 2013;**34**:2142−55.
3. McLaughlan JR, Harput S, Abou-Saleh RH, Peyman SA, Evans S, Freear S. Characterisation of liposome-loaded microbubble populations for subharmonic imaging. *Ultrasound Med Biol* 2017;**43**:346−56.
4. Aliabouzar M, Zhang LG, Sarkar K. Lipid coated microbubbles and low intensity pulsed ultrasound enhance chondrogenesis of human mesenchymal stem cells in 3d printed scaffolds. *Sci Rep* 2016;**6**:37728.
5. Jang Y, Kim D, Lee H, Jang H, Park S, Kim GE, et al. Development of an ultrasound triggered nanomedicine-microbubble complex for chemo-photodynamic-gene therapy. *Nanomedicine* 2020;**27**:102194.
6. Stride E. Physical principles of microbubbles for ultrasound imaging and therapy. *Cerebrovasc Dis* 2009;**27**(**Suppl 2**):1−13.
7. Doinikov AA, Haac JF, Dayton PA. Resonance frequencies of lipid-shelled microbubbles in the regime of nonlinear oscillations. *Ultrasonics* 2009;**49**:263−8.
8. Fan Z, Kumon RE, Deng CX. Mechanisms of microbubble-facilitated sonoporation for drug and gene delivery. *Ther Deliv* 2014;**5**:467−86.
9. Wang M, Zhang Y, Cai C, Tu J, Guo X, Zhang D. Sonoporation-induced cell membrane permeabilization and cytoskeleton disassembly at varied acoustic and microbubble-cell parameters. *Sci Rep* 2018;**8**:3885.
10. Rinaldi L, Folliero V, Palomba L, Zannella C, Isticato R, Di Francia R, et al. Sonoporation by microbubbles as gene therapy approach against liver cancer. *Oncotarget* 2018;**9**:32182−90.
11. Meng L, Liu X, Wang Y, Zhang W, Zhou W, Cai F, et al. Sonoporation of cells by a parallel stable cavitation microbubble array. *Adv Sci* 2019;**6**:1900557.
12. Okada K, Kudo N, Niwa K, Yamamoto K. A basic study on sonoporation with microbubbles exposed to pulsed ultrasound. *J Med Ultrason* 2001;**32**:3−11. 2005.
13. Perera R, Hernandez C, Cooley M, Jung O, Jeganathan S, Abenojar E, et al. Bubble trouble: conquering microbubble limitations in contrast enhanced ultrasound imaging by nature-inspired ultrastable echogenic nanobubbles. *bioRxiv* 2019:633578.
14. Alter J, Sennoga CA, Lopes DM, Eckersley RJ, Wells DJ. Microbubble stability is a major determinant of the efficiency of ultrasound and microbubble mediated *in vivo* gene transfer. *Ultrasound Med Biol* 2009;**35**:976−84.
15. Abou-Saleh RH, Peyman SA, Johnson BRG, Marston G, Ingram N, Bushby R, et al. The influence of intercalating perfluorohexane into lipid shells on nano and microbubble stability. *Soft Matter* 2016;**12**:7223−30.
16. Kwan JJ, Borden MA. Lipid monolayer collapse and microbubble stability. *Adv Colloid Interface Sci* 2012;**183−184**:82−99.
17. Unger EC, Porter T, Culp W, Labell R, Matsunaga T, Zutshi R. Therapeutic applications of lipid-coated microbubbles. *Adv Drug Deliv Rev* 2004;**56**:1291−314.
18. Segers T, Lassus A, Bussat P, Gaud E, Frinking P. Improved coalescence stability of monodisperse phospholipid-coated microbubbles formed by flow-focusing at elevated temperatures. *Lab Chip* 2018;**19**:158−67.
19. Chen Y, Liang Y, Jiang P, Li F, Yu B, Yan F, et al. Lipid/PLGA hybrid microbubbles as a versatile platform for noninvasive image-guided targeted drug delivery. *ACS Appl Mater Interfaces* 2019;**11**:41842−52.
20. Yan P, Chen KJ, Wu J, Sun L, Sung HW, Weisel RD, et al. The use of MMP2 antibody-conjugated cationic microbubble to target the ischemic myocardium, enhance Timp3 gene transfection and improve cardiac function. *Biomaterials* 2014;**35**:1063−73.
21. Unnikrishnan S, Klibanov AL. Microbubbles as ultrasound contrast agents for molecular imaging: preparation and application. *AJR Am J Roentgenol* 2012;**199**:292−9.
22. Jeong S, Park JY, Cha MG, Chang H, Kim YI, Kim HM, et al. Highly robust and optimized conjugation of antibodies to nanoparticles using quantitatively validated protocols. *Nanoscale* 2017;**9**:2548−55.
23. Oliveira JP, Prado AR, Keijok WJ, Antunes PWP, Yapuchura ER, Guimarães MCC. Impact of conjugation strategies for targeting of antibodies in gold nanoparticles for ultrasensitive detection of 17β-estradiol. *Sci Rep* 2019;**9**:1−8.
24. Kumeda N, Ogawa Y, Akimoto Y, Kawakami H, Tsujimoto M, Yanoshita R. Characterization of membrane integrity and morphological stability of human salivary exosomes. *Biol Pharm Bull* 2017;**40**:1183−91.
25. Han H, Lee H, Kim K, Kim H. Effect of high intensity focused ultrasound (HIFU) in conjunction with a nanomedicines-microbubble complex for enhanced drug delivery. *J Control Release* 2017;**266**:75−86.

26. Kim H, Lee H, Moon H, Kang J, Jang Y, Kim D, et al. Resonance-based frequency-selective amplification for increased photoacoustic imaging sensitivity. *ACS Photonics* 2019;**6**:2268−76.

27. Sirsi S, Borden M. Microbubble compositions, properties and biomedical applications. *Bubble Sci Eng Technol* 2009;**1**:3−17.

28. Roovers S, Segers T, Lajoinie G, Deprez J, Versluis M, De Smedt SC, et al. The role of ultrasound-driven microbubble dynamics in drug delivery: from microbubble fundamentals to clinical translation. *Langmuir* 2019;**35**:10173−91.

29. Doyle LM, Wang MZ. Overview of extracellular vesicles, their origin, composition, purpose, and methods for exosome isolation and analysis. *Cells* 2019;**8**:727.

30. Andreu Z, Yanez-Mo M. Tetraspanins in extracellular vesicle formation and function. *Front Immunol* 2014;**5**:442.

31. Flecha FLG. Kinetic stability of membrane proteins. *Biophys Rev* 2017;**9**:563−72.

32. Qin S, Ferrara KW. The natural frequency of nonlinear oscillation of ultrasound contrast agents in microvessels. *Ultrasound Med Biol* 2007;**33**:1140−8.

33. Upadhyay A, Dalvi SV. Microbubble formulations: synthesis, stability, modeling and biomedical applications. *Ultrasound Med Biol* 2019;**45**:301−43.

34. Fowler PW, Helie J, Duncan A, Chavent M, Koldso H, Sansom MSP. Membrane stiffness is modified by integral membrane proteins. *Soft Matter* 2016;**12**:7792−803.

35. Agrawal H, Zelisko M, Liu LP, Sharma P. Rigid proteins and softening of biological membranes-with application to HIV-induced cell membrane softening. *Sci Rep* 2016;**6**:25412.

36. Schroeder A, Kost J, Barenholz Y. Ultrasound, liposomes, and drug delivery: principles for using ultrasound to control the release of drugs from liposomes. *Chem Phys Lipids* 2009;**162**:1−16.

37. Sugano M, Negishi Y, Endo-Takahashi Y, Suzuki R, Maruyama K, Yamamoto M, et al. Gene delivery system involving bubble liposomes and ultrasound for the efficient *in vivo* delivery of genes into mouse tongue tissue. *Int J Pharm* 2012;**422**:332−7.

38. Ibsen S, Benchimol M, Simberg D, Schutt C, Steiner J, Esener S. A novel nested liposome drug delivery vehicle capable of ultrasound triggered release of its payload. *J Control Release* 2011;**155**:358−66.

39. Karshafian R, Bevan PD, Williams R, Samac S, Burns PN. Sonoporation by ultrasound-activated microbubble contrast agents: effect of acoustic exposure parameters on cell membrane permeability and cell viability. *Ultrasound Med Biol* 2009;**35**:847−60.

40. Drake CG, Lipson EJ, Brahmer JR. Breathing new life into immunotherapy: review of melanoma, lung and kidney cancer. *Nat Rev Clin Oncol* 2014;**11**:24−37.

41. Nam J, Son S, Park KS, Zou WP, Shea LD, Moon JJ. Cancer nanomedicine for combination cancer immunotherapy. *Nat Rev Mater* 2019;**4**:398−414.

42. Garg AD, Krysko DV, Vandenabeele P, Agostinis P. Hypericin-based photodynamic therapy induces surface exposure of damage-associated molecular patterns like HSP70 and calreticulin. *Cancer Immunol Immunother* 2012;**61**:215−21.

43. Morais JAV, Almeida LR, Rodrigues MC, Azevedo RB, Muehlmann LA. The induction of immunogenic cell death by photodynamic therapy in B16F10 cells *in vitro* is effected by the concentration of the photosensitizer. *Photodiagnosis Photodyn Ther* 2021;**35**:102392.

44. Shimizu K, Iyoda T, Okada M, Yamasaki S, Fujii SI. Immune suppression and reversal of the suppressive tumor microenvironment. *Int Immunol* 2018;**30**:445−55.

45. Whiteside TL. Immune suppression in cancer: effects on immune cells, mechanisms and future therapeutic intervention. *Semin Cancer Biol* 2006;**16**:3−15.